Ocean Engineering 351 (2026) 124312

Contents lists available at ScienceDirect

Ocean Engineering

journal homepage: www.elsevier.com/locate/oceaneng

Research paper

Data-driven condition monitoring of mooring systems: A demonstration with the M4 multi-float wave energy converter

Heng Yang, Long Zhang *, Peter Stansby, Samuel Draycott

School of Engineering, University of Manchester, Manchester, UK

ARTICLE INFO

Keywords:
Wave energy converter
Mooring line force
Data-driven method
Condition monitoring

ABSTRACT

Monitoring the condition of mooring systems is essential for the safe operation and timely maintenance of floating platforms including wave energy converters (WECs). However, mooring dynamics are highly nonlinear due to nonlinearities in wave forcing, marine growth effects on floater and mooring cables or chains, WEC dynamics, synthetic cable or chain nonlinearity, and floater-mooring coupling. These effects reduce the effectiveness of linear system identification methods and make accurate condition assessment challenging. In this study, we introduce a data-driven approach for condition monitoring that uses dynamic modelling to address these challenges. The method enables continuous monitoring, allowing gradual or sudden changes to be detected and faults addressed promptly. A time-delay neural network (TDNN) with Bayesian regularization backpropagation is employed to model the system's behaviour. Its performance is comprehensively compared with four popular models. The approach is validated using two surrogate fault scenarios: (i) two different mooring configurations tested in the same basin, and (ii) nominally identical configurations tested in two different basins. Using six-degree-of-freedom (6-DOF) motion data, the approach is demonstrated to identify the fault condition for all sea states under both scenarios, demonstrating the robustness and sensitivity for subtle changes, for unseen and complex conditions.

1. Introduction

Offshore renewable energy is increasingly recognised as a key component of global electricity generation for the coming decades. The reliability of the mooring systems used in floating offshore energy projects is a major concern. High failure rates in mooring systems have been reported (Kvitrud, 2014). These failures compromise the structural integrity and operational reliability and also lead to substantial financial losses, and have the potential to reduce confidence in the technologies. Therefore, condition monitoring of operational mooring systems is highly desirable to detect early faults and prevent catastrophic failures.

The vast majority of existing work uses simulation models for the purpose of developing and validating different condition monitoring algorithms. The popular simulation tools including OrcaFlex, Ansys and FAST are often used to simulate the mooring system response under healthy and damaged conditions. The direct comparison of the time or frequency responses of motions or forces have been investigated for severe failures (such as broken lines) (Chung et al., 2021). These direct comparisons may be limited to discrete normal and severely faulty conditions. Although linear system identification methods can be applied, they may be inadequate for continuous monitoring because of the nonlinear relationship between the mooring responses and the wave input (Zhang et al., 2024). In addition, nonlinear interactions play a critical role in floating systems, and recent studies have provided detailed physical insight into such coupled behaviours (Haider et al., 2025), further highlighting the need for data-driven approaches capable of modelling such complexities. Neural network-based approaches have therefore become popular choices for continuous mooring condition monitoring (Hashmani et al., 2024). The Radial Basis Function (RBF) neural networks have been proposed to identify damage arising from the complex interactions between the floater and mooring system (Wang et al., 2020). A Deep Neural Network (DNN)-based structural health monitoring system has been proposed to identify damaged mooring lines in tension leg platforms (TLPs) (Chung et al., 2020). Multilayer Perceptron (MLP) and Long Short-Term Memory (LSTM) networks have been proposed to enable near real-time detection of mooring line failures (Saad et al., 2021). Recurrent Neural Networks (RNNs) have been proposed for detecting catenary mooring line damage, including small-scale local defects (Lee et al., 2021). Convolutional Neural Network combined with t-distributed Stochastic Neighbour Embedding (CNN-t-SNE) has been developed to automatically identify the damage magnitude of

* Corresponding author.
E-mail address: long.zhang@manchester.ac.uk (L. Zhang).

https://doi.org/10.1016/j.oceaneng.2026.124312
Received 3 November 2025; Received in revised form 22 December 2025; Accepted 13 January 2026
Available online 20 January 2026
0029-8018/© 2026 The Author(s). Published by Elsevier Ltd. This is an open access article under the CC BY license (http://creativecommons.org/licenses/by/4.0/).

moorings based on the dynamic response of offshore platforms (Sun et al., 2023). These neural network algorithms have powerful capacities in modelling different types of time-frequency variations and nonlinearity under different types and severity of faults. In addition, a novel data-driven framework leveraging the ConvMamba architecture which combines convolutional operations with the Mamba state space model (SSM) architecture was introduced for continuous health monitoring and damage localization of mooring lines, exhibiting superior performance in terms of accuracy and computational efficiency (Mao et al., 2025).

However, most studies require a large amount of data for training and validation of condition monitoring methods, which are generally numerical wave-structure-mooring interaction modelling. The algorithms developed using these simulation data alone may not work well for real systems due to the idealization and approximation in the models. Due to the scarcity of data from real systems, especially in the early stages of deploying offshore renewable energy, there is limited research using experimental data (Ren et al., 2024). Recent work addressed this issue by employing a hierarchical variational autoencoder (HVAE) with diffusion modelling to generate damage data for various sea states from real healthy signals, and by leveraging both healthy and generated damage data for health monitoring (Fathnejat and Nava, 2025). However, its performance declines in highly nonlinear conditions, limiting its generalization to complex real-world scenarios. Moreover, fully supervised and weakly supervised shallow and deep learning models were developed for real-time health monitoring of mooring systems using a very limited amount of experimental data, while having challenges related to environmental robustness and sensor performance (Coraddu et al., 2024).

In this study, for the first time, a cost-effective data-driven system identification approach is proposed for monitoring the mooring condition of a floating platform using a generalized model trained by limited amount of measured motion and force data. We apply this to the relatively complex case of the multi-float wave energy converter M4, the development of which has been reviewed in recent work (Stansby and Draycott, 2024). The motion data consists of six degrees of freedom (6-DOF): surge (X), sway (Y), heave (Z), yaw (θ_Z), pitch (θ_Y), and roll (θ_X). The force exhibits a nonlinear relationship with the motion input, which can be effectively approximated by a dynamic model using limited experimental data. This results in a low computational demand and limited data requirements. Further, unlike most of existing work where only simulation data are used, we evaluate the effectiveness of the proposed method on a real mooring system from the multi-float M4 using experimental data under a wide range of wave conditions including directionally spread and crossing seas representing complex realistic open ocean conditions (Draycott et al., 2023). This condition monitoring approach is not limited to the M4 multi-float wave energy converter. The methodology that trains a generalized dynamic model from limited measured input and output data can be applied to a wide range of floating structures, including floating wind turbines, pontoons, and other wave energy devices. For these systems with nonlinear interactions, the approach can enable efficient monitoring and condition assessment of mooring lines or other structural components. The low computational demand and limited data requirements make it particularly suitable for early-stage fault detection and catastrophic-failure prevention. Moreover, because the method is grounded in real experimental measurements, it can adapt to different configurations and platform types, offering a flexible approach for real-world applications.

The paper is structured as follows. Section 2 introduces the proposed method. Section 3 presents the experimental set-up, followed by results in Section 4 and brief conclusions offered in Section 5.

2. Data-driven condition monitoring method

In this paper, a data-driven condition monitoring method is proposed using two steps illustrated in Fig. 1. The first step is to determine a normalized root-mean-square error (NRMSE) threshold based on data from the system operating under healthy conditions. The second step is to use this threshold to identify whether a changed system is operating in a faulty condition.

For the first step, the relationship between the input and output is modelled using a system identification (SI) approach, resulting in a generalized model representing all healthy cases. For each healthy case, the residual e_h defined as the difference between the predicted output and the measured output is computed, and the corresponding NRMSE values are obtained from these residuals by root-mean-square error (RMSE) calculation and normalization. By comparing all NRMSE values, an appropriate NRMSE threshold is selected.

In the second step, the measured output of the changed system is compared with the output predicted by the identified model to compute the NRMSE for each case. These calculated NRMSE values are then compared with the established threshold to determine whether the changed system is in a healthy or faulty condition.

2.1. Linear modelling

Although the relationship between motion and force is inherently nonlinear, a linear Autoregressive with exogenous input (ARX) model can still be employed as an approach can still be used to identify the mooring system and serve as a baseline for comparison with nonlinear methods. The general formulation of the ARX model is given by Ljung (1999):

$$y(n) = a_1 y(n-1) + \ldots + a_m y(n-m) + b_1 x(n-1) + \ldots + b_l x(n-l) + \xi(n) \tag{1}$$

where the pair set $\{x(n), y(n)\}$ represents input (motion) and output (force) at time interval n, $n = 1, \ldots, N$, N being the size of the training dataset. l and m represent the largest input and output lags, respectively. $\xi(n)$ denotes the error. This ARX model indicates that past input and output values have an effect on the current output value and can be used jointly to predict the future output.

2.2. Nonlinear modelling

Nonlinear modelling is expected to provide better performance. Several types of neural networks are commonly used for modelling time-series data, including Time Delay Neural Networks (TDNN), Radial Basis Function (RBF) Networks, Long Short-Term Memory (LSTM) Networks, and Generalized Regression Neural Networks (GRNN). In this paper, these methods are employed and compared to determine the most suitable model.

The general formulation of the TDNN is given by Liu et al. (2020):

$$h_j(n) = \phi(\sum_{i=1}^{d+1} w_{h,ji} x(n-i+1) + b_{h,j}) \tag{2}$$

$$y(n) = \sum_{j=1}^{m} w_{y,j} h_j(n) + b_y \tag{3}$$

where h is hidden layer output, d is the maximum delay and m is the number of hidden neurons, w and b are the weights and biases respectively, $\phi(\cdot)$ is the activation function. Similar to the ARX model, which relies on historical input and output data to predict current outputs, the TDNN utilizes time-delayed input signals to capture and model the system's temporal dynamics.

The general formulation of the RBF is given by Broomhead and Lowe (1988):

$$y(n) = \sum_{i=1}^{k} w_i \psi(\|x(n) - c_i\|) + b \tag{4}$$

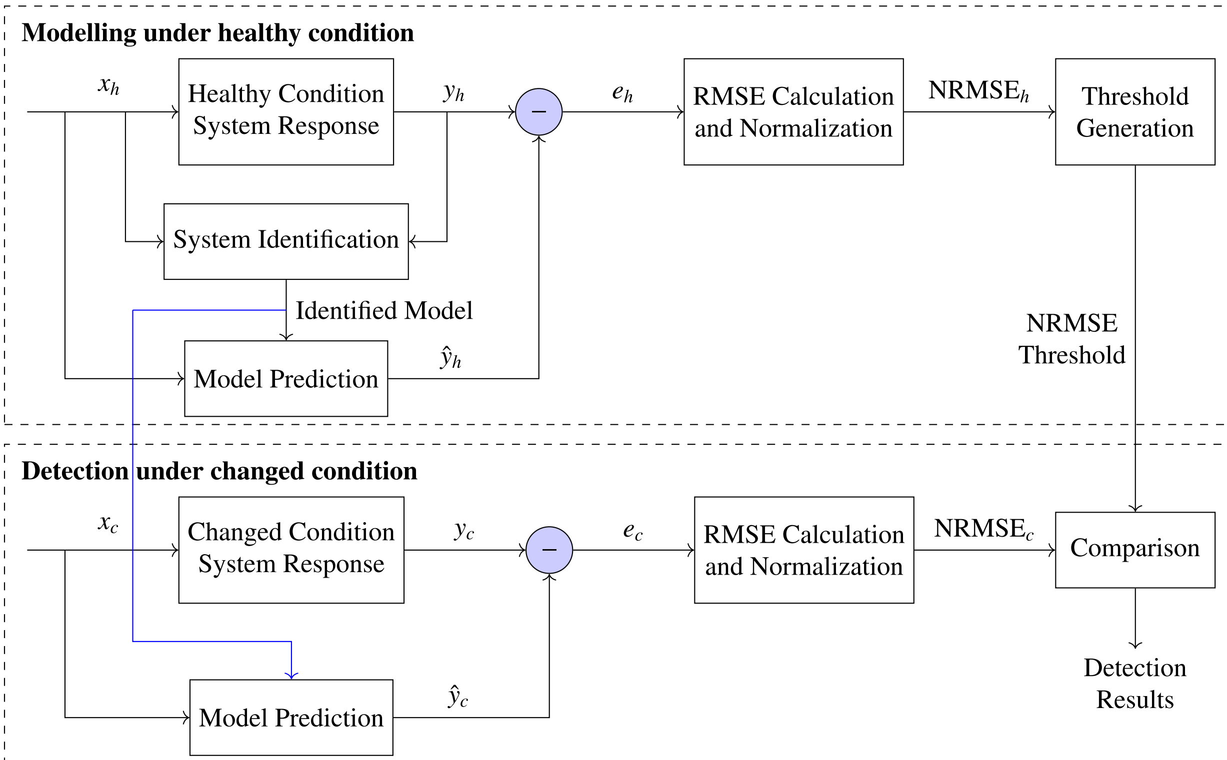

Fig. 1. The flowchart diagram of the proposed method (x and y are the input and output of system, $\hat{y}$ is the predicted output, e is the residual, subscript h and c indicate the variable under healthy and changed conditions, respectively.).

where k is the total number of radial basis functions in the network, and c_i are the centres of the RBFs. w_i is weight associated with the i-th radial basis function, and b is the bias term. $\psi(\cdot)$ is the radial basis function. Unlike ARX and TDNN models which depend on time delays or temporal structures, RBF networks instead use nonlinear basis functions to directly transform inputs into outputs. In principle, this allows them to model complex relationships without explicitly accounting for time dependencies.

The general formulation of the LSTM is given by Hochreiter and Schmidhuber (1997):

$$f_j(n) = \phi(w_{f,j}x(n) + \sum_{k=1}^{m} u_{f,jk}h_k(n-1) + b_{f,j}) \tag{5}$$

$$g_j(n) = \phi(w_{g,j}x(n) + \sum_{k=1}^{m} u_{g,jk}h_k(n-1) + b_{g,j}) \tag{6}$$

$$o_j(n) = \phi(w_{o,j}x(n) + \sum_{k=1}^{m} u_{o,jk}h_k(n-1) + b_{o,j}) \tag{7}$$

$$\tilde{c}_j(n) = \phi(w_{c,j}x(n) + \sum_{k=1}^{m} u_{c,jk}h_k(n-1) + b_{c,j}) \tag{8}$$

$$c_j(n) = f_j(n) \cdot c_j(n-1) + g_j(n) \cdot \tilde{c}_j(n) \tag{9}$$

$$h_j(n) = o_j(n) \cdot \tanh(c_j(n)) \tag{10}$$

$$y(n) = \sum_{j=1}^{m} w_{y,j}h_j(n) + b_y \tag{11}$$

where f is the forget gate, g is the input gate and o is the output gate. c is the cell state and h is the hidden state. m is the number of hidden units in the LSTM block. While ARX, TDNN, and RBF models use fixed memory or static functions, LSTM networks utilize adaptive memory cells capable of retaining information over extended periods, making them well-suited for capturing long-term dependencies in time series data.

The general formulation of the GRNN is given by Specht (1991):

$$y(n) = \frac{\sum_{n=1}^{N} \exp\left(-\frac{\|x(n)-x_{train}(n)\|^2}{2\sigma^2}\right) y_{train}(n)}{\sum_{n=1}^{N} \exp\left(-\frac{\|x(n)-x_{train}(n)\|^2}{2\sigma^2}\right)} \tag{12}$$

where the pair set $\{x_{train}(n), y_{train}(n)\}$ represents input (motion) and output (force) at time interval n, $n = 1, \dots, N$, N being the size of the training dataset. The pair set $\{x(n), y(n)\}$ represents the associated predicted dataset. σ is the smoothing parameter that determines the width of the Gaussian function. Unlike other models like ARX or TDNN, the GRNN computes outputs as a weighted average of training targets, with weights determined by the Gaussian distance metrics between the current and training inputs.

2.3. RMSE calculation and normalization

When training neural networks, the model often minimizes the Root Mean Square Error (RMSE), which is given by:

$$\text{RMSE} = \sqrt{\frac{1}{N}\sum_{n=1}^{N}(y(n) - \hat{y}(n))^2} = \sqrt{\frac{1}{N}e^T e} \tag{13}$$

where $y(n)$ and $\hat{y}(n)$ are measured output and predicted output are time interval n. $e = [\xi(1), \xi(2), \dots, \xi(N)]^T$ is the residual vector.

Different datasets may exhibit varying ranges and energy levels. To facilitate a fair comparison of RMSE across these datasets, normalization can be applied. The normalized RMSE is given by:

$$\text{NRMSE} = \frac{\text{RMSE}}{\text{std}(\mathbf{y})} \tag{14}$$

where std(·) denotes the standard deviation and $\mathbf{y} = [y(1), y(2), \ldots, y(N)]^T$ is the output vector.

2.4. NRMSE threshold and detection results

The NRMSE threshold is an indicator used to determine whether the system is operating under healthy or faulty conditions. It is obtained by comparing all NRMSE values recorded across different cases during healthy operation. Under healthy conditions, the NRMSE values lie within a specific range:

$$\mathrm{NRMSE}_h \in \left[\mathrm{NRMSE}_h^{\min}, \mathrm{NRMSE}_h^{\max}\right] \tag{15}$$

where $\mathrm{NRMSE}_h^{\min}$ and $\mathrm{NRMSE}_h^{\max}$ are the maximum and minimum NRMSE values under healthy conditions.

The NRMSE threshold can be defined as:

$$\mathrm{NRMSE}_{\mathrm{th}} = \mathrm{NRMSE}_h^{\max} + \delta \tag{16}$$

where δ represents the allowable tolerance of the system, related to the sensitivity of the method. The choice of δ has important practical implications. A too large δ reduces the sensitivity of the method, causing minor or early-stage faults to go undetected. On the other hand, a very small δ makes the method sensitive to minor environmental changes lead to false alarms even when the system is healthy. Therefore, δ must balance being robust to normal environmental changes while remaining sensitive enough to detect real system faults.

For a changed system, the NRMSE values fall within the range:

$$\mathrm{NRMSE}_c \in \left[\mathrm{NRMSE}_c^{\min}, \mathrm{NRMSE}_c^{\max}\right] \tag{17}$$

where $\mathrm{NRMSE}_c^{\min}$ and $\mathrm{NRMSE}_c^{\max}$ are the maximum and minimum NRMSE values for the changed system. If the minimum NRMSE of the changed system is less than the threshold, the system is considered to be in a faulty condition; otherwise, it is classified as healthy.

2.5. Training methods

For neural networks, different training algorithms can lead to varying convergence speeds and accuracies. Therefore, multiple training methods are employed and compared in this study to identify the most suitable solution. The update formulation of the trainable parameter for Levenberg-Marquardt backpropagation (trainlm) is given by Sapna et al. (2008):

$$\theta_{k+1} = \theta_k - (J^T J + \lambda I) J^T e_k \tag{18}$$

where θ is the trainable parameter and e is the error vector. J is Jacobian matrix of the network errors with respect to trainable parameter. λ is damping parameter and I is identity matrix.

The update formulation of the trainable parameter for Resilient backpropagation (trainrp) is given by Gnther and Fritsch (2010):

$$E_k = \frac{1}{2N}\sum_{n=1}^{N}(y(n) - \hat{y}(n))^2 = \frac{1}{2N} e_k^T e_k \tag{19}$$

$$\Delta_k = \begin{cases} \eta^+ \cdot \Delta_{k-1} & \text{if } \frac{\partial E_{k-1}}{\partial \theta_{k-1}} \cdot \frac{\partial E_k}{\partial \theta_k} > 0 \\ \eta^- \cdot \Delta_{k-1} & \text{if } \frac{\partial E_{k-1}}{\partial \theta_{k-1}} \cdot \frac{\partial E_k}{\partial \theta_k} < 0 \\ \Delta_{k-1} & \text{otherwise} \end{cases} \tag{20}$$

$$\theta_{k+1} = \theta_k - \mathrm{sign}\left(\frac{\partial E_k}{\partial \theta_k}\right) \cdot \Delta_k \tag{21}$$

where E is the loss function. Δ is updating step for trainable parameter. η^+ and η^- are step-size increase factor and step-size decrease factor. sign(·) is the sign function returns $+1$ or -1.

The update formulation of the trainable parameter for Gradient descent with momentum backpropagation (traingdm) is given by Nayak et al. (2016):

$$v_k = \gamma v_{k-1} + \alpha \frac{\partial E_k}{\partial \theta_k} \tag{22}$$

$$\theta_{k+1} = \theta_k - v_k \tag{23}$$

where v is the momentum. γ is momentum coefficient and α is learning rate.

The update formulation of the trainable parameter for Broyden-Fletcher-Goldfarb-Shanno (BFGS) quasi-Newton backpropagation (trainbfg) is given by Robitaille et al. (1996):

$$s_k = \theta_k - \theta_{k-1} \tag{24}$$

$$y_k = \nabla E(\theta_k) - \nabla E(\theta_{k-1}) \tag{25}$$

$$H_k = \left(I - \frac{s_k y_k^T}{y_k^T s_k}\right) H_{k-1} \left(I - \frac{y_k s_k^T}{y_k^T s_k}\right) + \frac{s_k s_k^T}{y_k^T s_k} \tag{26}$$

$$\theta_{k+1} = \theta_k - H_k \nabla E(\theta_k) \tag{27}$$

where s is the step taken in parameter space and y is the change in the gradient. H is the approximation of the inverse Hessian matrix. $\nabla E(\theta)$ is the gradient of the error function with respect to the trainable parameter.

The update formulation of the trainable parameter for Scaled conjugate gradient backpropagation (trainscg) is given by Müller (1993):

$$g_k = \nabla E(\theta_k) \tag{28}$$

$$p_k = g_k + \beta_k p_{k-1} \tag{29}$$

$$\beta_k = \frac{g_k^\top (g_k - g_{k-1})}{g_{k-1}^T g_{k-1}} \tag{30}$$

$$s_k = \frac{\nabla E(\theta_k + \sigma_k p_k) - g_k}{\sigma_k} \tag{31}$$

$$\alpha_k = -\frac{g_k^T p_k}{p_k^\top s_k} \tag{32}$$

$$\theta_{k+1} = \theta_k + \alpha_k p_k \tag{33}$$

where g is gradient, p is conjugate direction, β is conjugate coefficient, s is second derivative (Hessian) information and α is step size.

The update formulation of the trainable parameter for Bayesian regularization backpropagation (trainbr) is given by Burden and Winkler (2009):

$$E_k = \beta E_D + \alpha E_W \tag{34}$$

$$E_D = \sum_{n=1}^{N}(y(n) - \hat{y}(n))^2 = e_k^T e_k \tag{35}$$

$$E_W = \theta_k^T \theta_k \tag{36}$$

$$\theta_{k+1} = \theta_k - \eta \nabla E(\theta_k) \tag{37}$$

where β and α are data error parameter and regularization parameter. E_D and E_W are data error term and weight penalty term. η is the learning rate.

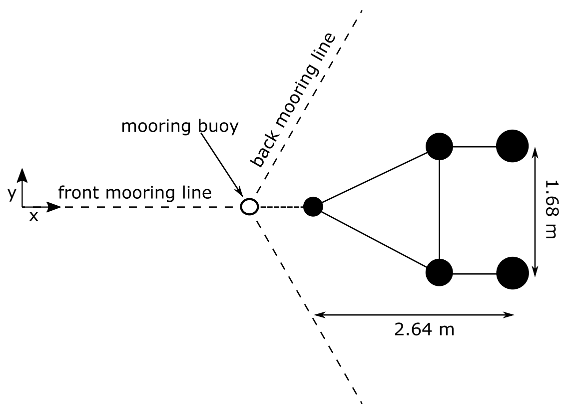

Fig. 2. Top view of the layout of the M4 WEC and mooring configuration 1.

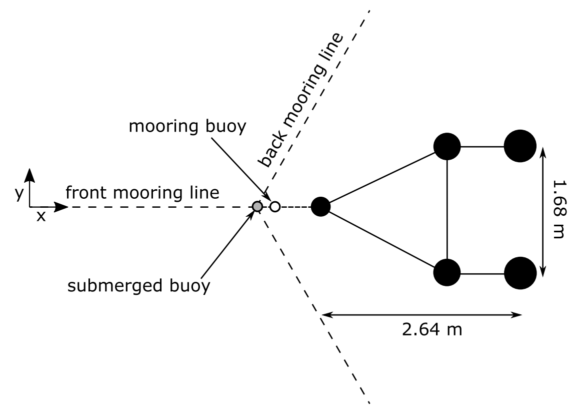

Fig. 4. Top view of the layout of the M4 WEC and mooring configuration 2.

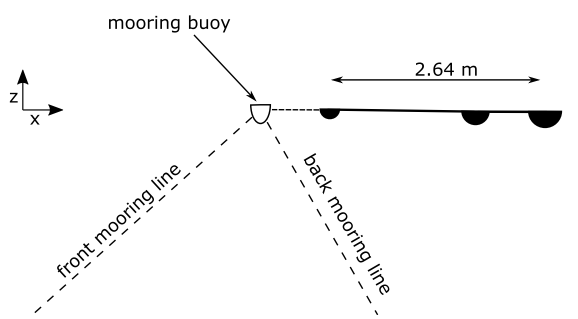

Fig. 3. Side-on view of the layout of the M4 WEC and mooring configuration 1.

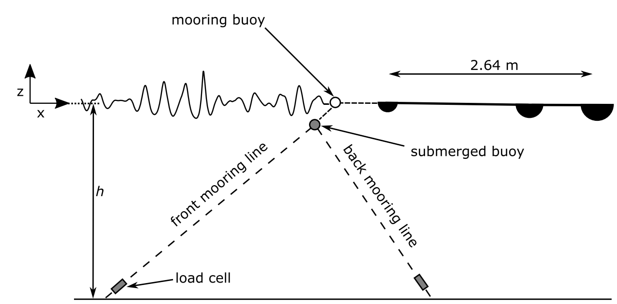

Fig. 5. Side-on view of the layout of the M4 WEC and mooring configuration 2. $h = 2$ m is the water depth.

3. Experimental set-up

In this study, the M4 WEC system is composed of five floats: one bow float, two mid-floats, and two stern floats. Two mooring configurations with minor differences, named as Configuration 1 and Configuration 2, are used to emulate the normal and abnormal conditions, respectively. Configuration 1 has a 0.2 m diameter hemispherical buoy weighing 1.25 kg, connected to the seabed with three elastic cables and connected to the bow float with one elastic cable, as shown in Figs. 2 and 3. Configuration 2, as shown in Figs. 4 and 5, features a small surface mooring buoy (0.11 m diameter) connected to a submerged buoy (0.15 m diameter weighing 0.21 kg) also connected with three similar elastic cables. The mooring cable consisted of two latex rubber (exercise) bands (each 0.4 m long unstretched) in series in the lower part (1.2 m length total) with an inelastic nylon cord to the buoy. The nominal stiffness is 65 N/m with weak nonlinearity (Draycott et al., 2023). Both configurations show similar behaviour; however, it was found that compared to Configuration 1, the anchor forces of Configuration 2 at the wave frequencies were reduced but the low-frequency forces increased (Draycott et al., 2023). The different dynamics observed make them suitable scenarios for validating condition monitoring algorithms designed for change detection.

Our study utilizes two sets of experimental results to address complementary research objectives and enhance the robustness of the method, one set used to monitor two slightly mooring configurations in identical sea states, and one set used to monitor the nominally same configuration in different facilities. The first set was obtained from wave basin experiments conducted at the COAST laboratory at the University of Plymouth, UK, with the water depth set to 2 m. Both Configuration 1 and 2 are tested. Fig. 6 shows the M4 WEC and its mooring system in the wave basin experiment. The experiments were conducted under 22 irregular wave conditions, each with a duration of 35 min (2100 s). The 6-DOF M4 motions were recorded using a Qualisys motion capture camera system, and Futek submersible load cells were used to measure the mooring line loads. Qualisys motion capture camera system is sampled at 128 Hz, and Futek submersible load cells are sampled at 1613 Hz. Since the data spectrum is dominated by low frequency components, both motion and force data are downsampled to 8 Hz (Zhang et al., 2024). This effectively serves as a low-pass filter while keeping both datasets at the same frequency. Qualisys displacements are expected to have sub-millimetre accuracy, and the submersible Futek load cells have approximately 1 N uncertainty with linearity within about 0.2 %. The Futek load cell measurements contain minor high-frequency noise, which is removed by downsampling. The conditions are defined in Table 1. The first eleven cases involved varying combinations of significant wave heights (H_s) and peak periods (T_p), with four levels of H_s (0.06 m, 0.09 m, 0.13 m, and 0.16 m) and three values of T_p (1.2 s, 1.4 s, and 1.8 s). An additional case featured a larger wave height of $H_s = 0.24$ m with $T_p = 1.8$ s. These conditions all use a constant peak enhancement factor ($\gamma = 3.3$), and have unidirectional incident wave conditions. Two additional cases are added to assess the sensitivity to the frequency bandwidth, where γ is set to values of 1 and 2. The remaining cases represent conditions with directional spreading (using a cos-2s spreading distribution, described further below).

The second set of experiments was conducted at the FloWave Ocean Energy Research Facility at the University of Edinburgh, where only Configuration 2 is tested (although with slight differences in line lengths and angles due to different bed-mounting points). The sensors have similar settings to those used in the COAST experiments; however, the load cell measurements are sampled at 128 Hz. This set included 10 different wave conditions, also summarized in Table 1. Similar to the COAST experiments, these conditions were based on JONSWAP spectra all with $\gamma = 3.3$. Four cases are unidirectional, with the remaining being directionally spread, with some bi-model 'crossing' conditions, and are representative of more realistic and complex ocean conditions.

For all directionally spread conditions, we use a frequency-independent bi-modal directional spreading function $D(\theta)$ based on the

Table 1
Wave conditions for 32 cases in experiments.

COAST (Plymouth) : C FloWave (Edinburgh) : F					Crossing Angle	Config- uration	System Identification		Condition Monitoring	
Case	Hs (m)	Tp (s)	s (σ_θ)	γ	$\Delta\theta$	1,2	Train	Test	Train	Test
C1	0.06	1.2	∞ (0°)	3.3	0	1,2	/	1,2	2	1
C2	0.06	1.4	∞ (0°)	3.3	0	1,2	1,2	/	2	1
C3	0.06	1.8	∞ (0°)	3.3	0	1,2	1,2	/	2	1
C4	0.09	1.2	∞ (0°)	3.3	0	1,2	1,2	/	2	1
C5	0.09	1.4	∞ (0°)	3.3	0	1,2	/	1,2	2	1
C6	0.09	1.8	∞ (0°)	3.3	0	1,2	1,2	/	2	1
C7	0.13	1.2	∞ (0°)	3.3	0	1,2	1,2	/	2	1
C8	0.13	1.4	∞ (0°)	3.3	0	1,2	/	1,2	2	1
C9	0.13	1.8	∞ (0°)	3.3	0	1,2	1,2	/	2	1
C10	0.16	1.4	∞ (0°)	3.3	0	1,2	/	1,2	2	1
C11	0.16	1.8	∞ (0°)	3.3	0	1,2	1,2	/	2	1
C12	0.16	1.4	∞ (0°)	1	0	1,2	1,2	/	2	1
C13	0.16	1.4	∞ (0°)	2	0	1,2	1,2	/	2	1
C14	0.24	1.8	∞ (0°)	3.3	0	1,2	1,2	/	2	1
C15	0.13	1.2	25 (15.9°)	3.3	0	2	2	/	2	/
C16	0.13	1.2	10 (24.4°)	3.3	0	2	/	2	2	/
C17	0.13	1.2	5 (33.1°)	3.3	0	2	2	/	2	/
C18	0.16	1.4	25 (15.9°)	3.3	0	1,2	1,2	/	2	1
C19	0.16	1.4	10 (24.4°)	3.3	0	2	2	/	2	/
C20	0.16	1.4	5 (33.1°)	3.3	0	1,2	/	1,2	2	1
C21	0.24	1.8	25 (15.9°)	3.3	0	2	/	2	2	/
C22	0.24	1.8	10 (24.4°)	3.3	0	2	2	/	2	/
F1	0.06	1.8	∞ (0°)	3.3	0	2	2	/	/	2
F2	0.13	1.4	∞ (0°)	3.3	0	2	/	2	/	2
F3	0.16	1.4	∞ (0°)	3.3	0	2	2	/	/	2
F4	0.16	1.8	∞ (0°)	3.3	0	2	2	/	/	2
F5	0.13	1.4	5 (33.1°)	3.3	0	2	2	/	/	/
F6	0.13	1.4	10 (24.4°)	3.3	0	2	2	/	/	/
F7	0.13	1.4	25 (15.9°)	3.3	0	2	/	2	/	/
F8	0.13	1.4	25 (15.9°)	3.3	45	2	2	/	/	/
F9	0.13	1.4	25 (15.9°)	3.3	90	2	/	2	/	/
F10	0.13	1.4	25 (15.9°)	3.3	135	2	2	/	/	/

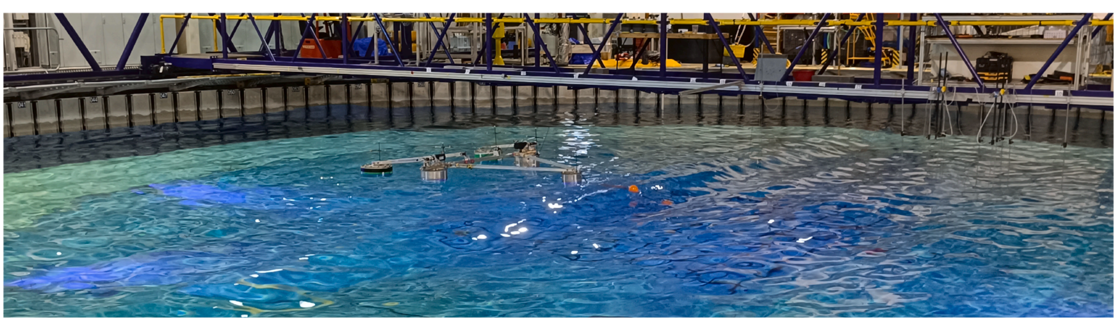

Fig. 6. A photo of the layout of the M4 WEC in the FloWave basin.

superposition of cos-2s spreading functions:

$$D(\theta) = \alpha_1 \left(\cos\left(\frac{\theta - \bar{\theta}_1}{2} \right) \right)^{2s_1} + \alpha_2 \left(\cos\left(\frac{\theta - \bar{\theta}_2}{2} \right) \right)^{2s_2} \tag{38}$$

where θ is the direction. For each mode i, $\bar{\theta}_i$ is the mean direction, and s_i parameter determines the directional spreading. The value α_i controls the amplitudes of the modes and is set to ensure that $\int_{-\pi}^{\pi} D(\theta) d\theta = 1$. For all crossing conditions tested, both modes were set to have equal directional spreading and equal amplitude and therefore $\alpha_1 = \alpha_2$ and $s_1 = s_2$. We also ensure the total mean direction is always equal to zero and therefore $\bar{\theta}_1 = -\bar{\theta}_2$ and the crossing angle $\Delta\theta = 2|\bar{\theta}_i|$. As per Table 1, we assess uni-modal spectra with s values of ∞, 5, 10 and 25, and bi-modal spectra with $s = 25$ and $\Delta\theta$ of 45°, 90° and 135°. For uni-modal spectra, this can be considered as either the special case that both modes have the same mean direction and directional spreading, or as a single mode. The s values in Eq. (38) and Table 1 can be converted to a standard deviation of an equivalent Gaussian directional distribution via $\sigma_\theta = \sqrt{2/(1+s)}$. These more physically interpretable values are also presented in Table 1.

4. Results

4.1. Model comparison and choice

Selecting the most suitable model is a critical step in the process. Both linear and nonlinear models are considered, including ARX, TDNN, RBF, LSTM, and GRNN. These models are compared based on performance, and the best-performing one is chosen. For these initial comparisons, during training, the first 70 % of the data from Case C1 in Configuration 2 are used for training, while the remaining 30 % are reserved for testing. The input of the model is the surge motion (X) of the bow float, and the output of the training data is the bed force measured by the front line (F_{front}). The prediction results are shown in Fig. 7, and the NRMSE results are compared and listed in Table 2. The ARX model shows slightly better prediction accuracy on the test set than on the training set due to under-fitting, but its overall prediction accuracy is limited by its linear structure, which cannot capture the system's nonlinear dynamics. The RBF model has poor accuracy because it cannot incorporate temporal dependencies, making it less effective

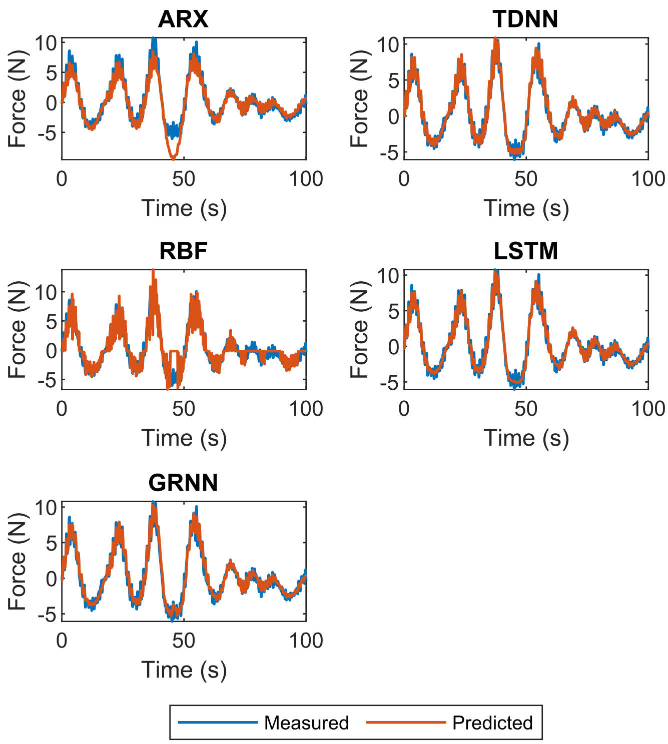

Fig. 7. Time series plot of predicted and measured force for different models on the test data from Configuration 2, Case C1.

Table 2
NRMSE results for Case C1 with different models.

Model	Linearity	Delay	Train	Test
ARX	Linear	Yes	0.2872	0.2485
TDNN	Nonlinear	Yes	**0.1143**	**0.1428**
RBF	Nonlinear	No	0.3875	0.3877
LSTM	Nonlinear	Yes	0.1416	0.1589
GRNN	Nonlinear	No	0.1430	0.1690

for dynamic systems. In contrast, nonlinear models with delay, such as TDNN and LSTM models, achieve much higher accuracy by effectively capturing both nonlinearities and system dynamics. Among nonlinear models without delay, GRNN model has better accuracy due to its more effective formulation and training mechanism; instead of storing only weights like RBF model, GRNN model retains all training samples, enabling better interpolation and generalization. Overall, the TDNN, LSTM, and GRNN models achieve better prediction accuracy than the ARX and RBF models, as indicated by their lower NRMSE values.

Although the LSTM and GRNN models achieve prediction accuracy comparable to the TDNN model, they are not the preferred choices. For the LSTM model, the model structure is more complex than TDNN model, makes training time significantly longer. Even for a single case with a single input DOF, LSTM requires about 7 minutes to train, while the TDNN completes the same task in only a few seconds. This implies that when training a generalized LSTM model across multiple cases and multiple input DOFs, the total computational cost becomes prohibitively large. For the GRNN model, all training samples must be stored explicitly, while the TDNN model only stores its learned weights. Therefore, when training a generalized GRNN model across multiple cases and multiple input DOFs, the required memory becomes excessively large. Due to its lower computational, memory requirements and better prediction accuracy, the TDNN model is selected as the preferred approach.

Different learning methods are evaluated to further improve the model's performance. Several training algorithms are compared, including Levenberg-Marquardt backpropagation (trainlm), Resilient backpropagation (trainrp), Gradient descent with momentum backpropagation (traingdm), Broyden-Fletcher-Goldfarb-Shanno (BFGS) quasi-Newton backpropagation (trainbfg), Scaled conjugate gradient backpropagation (trainscg), and Bayesian regularization backpropagation (trainbr). The training and test datasets remain 70 % and 30 % of the data from Case C1 in Configuration 2, respectively. The NRMSE results are listed in Table 3. Bayesian regularization backpropagation achieves the best performance and yields the smallest NRMSEs, and is therefore selected.

Table 3
NRMSE results for Case C1 with different learning methods.

Learning Method	Train	Test
trainlm	0.1165	0.1437
trainrp	0.1242	0.1518
traingdm	0.1385	0.1611
trainbfg	0.1191	0.1467
trainscg	0.1187	0.1452
trainbr	**0.1143**	**0.1428**

Table 4
NRMSE results for Case C1 with different activation functions.

Activation Function	Train	Test
logsig	0.1233	0.1502
tansig	**0.1143**	**0.1428**
softmax	0.1172	0.1447
elliotsig	0.1155	0.1433

Activation functions play an important role in the performance of the TDNN. Several functions, including the logsig, tansig, softmax, and elliotsig functions, can be used as activation functions in the TDNN. For each of these activation functions, using the same training and test datasets, the NRMSE results are listed in Table 4. The tansig function is selected as the activation function due to its moderately superior performance.

4.2. Input data selection

After determining the neural network type and training settings, the selection of input data for training is further considered. While surge motion is the primary motion driving mooring force, other motions also influence the resulting force, particularly for directional wave conditions. Different input configurations, including surge (X) motion only, planar (XY) motion, spatial (XYZ) motion, and full 6-DOF motion, are compared. The TDNN model is now generalized across all cases for each configuration and basin, and are trained using approximately 70 % of the total data from each configuration. For Configuration 1, training uses the data from eleven wave conditions, and testing uses the data from unseen five wave conditions. For Configuration 2, training uses data from fifteen wave conditions, and testing uses data from seven unseen conditions as listed in Table 1. For FloWave data, training uses data from seven wave conditions, with testing using data from three, see Table 1.

To evaluate the effect of different input configurations, the TDNN model is first applied to Configuration 1. The NRMSE results for different numbers of input variables in Configuration 1 are presented in Table 5. As the number of inputs increases, from surge only, to planar, spatial, and finally 6-DOF, the average NRMSE across all cases consistently decreases, with only a few cases showing a slight increase in NRMSE when moving from one to two inputs. The 6-DOF input yields the lowest average NRMSE, and all individual cases achieve their minimum error in this setting. Prediction results for this input configuration on the test dataset are shown in Fig. 8. The model demonstrates strong

Table 5
NRMSE Results for different input settings in Configuration 1. The generalized model is trained on all cases identified as "Train" and tested respectively on the cases identified as "Test".

Case	Set	X only	XY	XYZ	6-DOF
C1	Test	0.6911	0.6965	0.5964	0.5735
C2	Train	0.7952	0.7979	0.6497	0.6291
C3	Train	0.9049	0.9084	0.6829	0.6586
C4	Train	0.5617	0.5621	0.5127	0.4853
C5	Test	0.7303	0.7247	0.6023	0.5788
C6	Train	0.8616	0.8601	0.6312	0.6082
C7	Train	0.4913	0.4853	0.4574	0.4534
C8	Test	0.5849	0.5830	0.5059	0.4950
C9	Train	0.7930	0.7788	0.6136	0.6007
C10	Test	0.5368	0.5354	0.4546	0.4445
C11	Train	0.7329	0.7238	0.5804	0.5560
C12	Train	0.5234	0.5184	0.4611	0.4432
C13	Train	0.5254	0.5195	0.4528	0.4326
C14	Train	0.7274	0.7331	0.6651	0.6525
C18	Train	0.6198	0.6070	0.5252	0.5075
C20	Test	0.6222	0.6107	0.4762	0.4594
Average		0.6689	0.6653	0.5542	**0.5361**

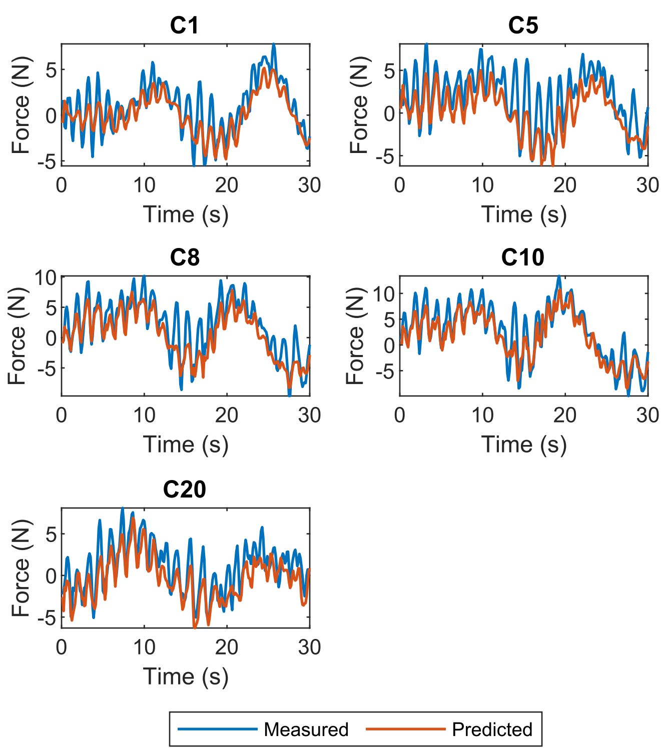

Fig. 8. Time series plot of predicted and measured force for test data when model input is 6-DOF motion in configuration 1.

predictive performance at low frequencies, though accuracy decreases at high frequencies.

To further validate the influence of input configurations, the same analysis is extended to Configuration 2. The NRMSE results for Configuration 2 are listed in Table 6. Overall, the average NRMSE is lower compared to Configuration 1. However, increasing the number of input variables from one to two leads to a slight rise in average NRMSE, increasing in most individual cases. When the number of inputs increases from two to three, the NRMSE decreases for many cases, lowering the average, though it remains slightly higher than with a single input. When all 6-DOF motions are used, a significant number of cases achieve their minimum NRMSE, resulting in the lowest average error. This suggests the rotations, mainly pitch (θ_y) are more important to capture for Configuration 2. Prediction results when the model input is 6-DOF motion are shown in Fig. 9, corresponding to the test dataset. At high frequencies, the model demonstrates improved accuracy compared to the Configuration 1 model, contributing to the overall lower NRMSE. However, in some cases, the performance at low frequencies is reduced, suggesting that the model is overfitting in these scenarios.

Table 6
NRMSE Results for different input setting in Configuration 2. The generalized model is trained on all cases identified as "Train" and tested respectively on the cases identified as "Test".

Case	Set	X only	XY	XYZ	6-DOF
C1	Test	0.3916	0.4056	0.3578	0.2559
C2	Train	0.4010	0.4209	0.3539	0.2415
C3	Train	0.4147	0.4999	0.3623	0.3703
C4	Train	0.3545	0.3551	0.3163	0.2510
C5	Test	0.4056	0.4033	0.3654	0.3081
C6	Train	0.3953	0.4213	0.3654	0.3063
C7	Train	0.2835	0.3000	0.2711	0.2209
C8	Test	0.2877	0.2967	0.2852	0.2878
C9	Train	0.4023	0.4449	0.4017	0.4045
C10	Test	0.2707	0.2822	0.2605	0.2440
C11	Train	0.3650	0.3906	0.3503	0.3130
C12	Train	0.2924	0.3015	0.2756	0.2024
C13	Train	0.2132	0.2142	0.2034	0.1977
C14	Train	0.3343	0.3607	0.3198	0.2335
C15	Train	0.2909	0.2944	0.2549	0.2574
C16	Test	0.3249	0.3402	0.3245	0.3442
C17	Train	0.3809	0.4106	0.3930	0.4701
C18	Train	0.4088	0.4570	0.4849	0.4708
C19	Train	0.3875	0.4191	0.4376	0.4125
C20	Test	0.4175	0.4812	0.5331	0.4599
C21	Test	0.3414	0.3677	0.3681	0.4368
C22	Train	0.4058	0.4438	0.4691	0.5331
Average		0.3532	0.3778	0.3525	**0.3283**

In order to assess the generalizability of the TDNN model for complex ocean conditions, the same input configuration analysis is conducted using the FloWave dataset. This dataset comprising complex crossing sea states where all degrees of freedom may be expected to be important. The NRMSE results for the FloWave dataset are listed in Table 7. In general, the average NRMSE decreases as more motion components are included in the model input. This trend is consistent across most cases. However, three cases show a different pattern. In Case F1, the NRMSE increases when the second motion component is added, then decreases slightly with the third component, though it remains higher than the result using only the primary surge motion. The lowest NRMSE is achieved when all motion components are included. In Case F2, the NRMSE initially increases with additional inputs, then decreases, but increases slightly when all six motion components are used. In Case F4, the NRMSE rises when the second motion component is introduced. These variations suggest that in some cases, including more input variables leads to overfitting, affecting the model's generalization. The patterns for the cases are similar to that observed in Configuration 2 in the COAST laboratory as intended. The predicted results for the test cases, when the model input includes all six motion components, are shown in Fig. 10. The model demonstrates good performance even for highly directional unseen cases including a good representation of the high frequency content.

4.3. *Condition monitoring performance*

4.3.1. *Configuration 1 vs. configuration 2*

For condition monitoring, the first experiment focuses on monitoring two configurations in the COAST laboratory. TDNN models are trained using data from Configuration 2, which represents the healthy condition, and tested on data from Configuration 1, representing the faulty condition. To assess the physical differences between the configurations we present Fast Fourier Transforms (FFTs) of the surface

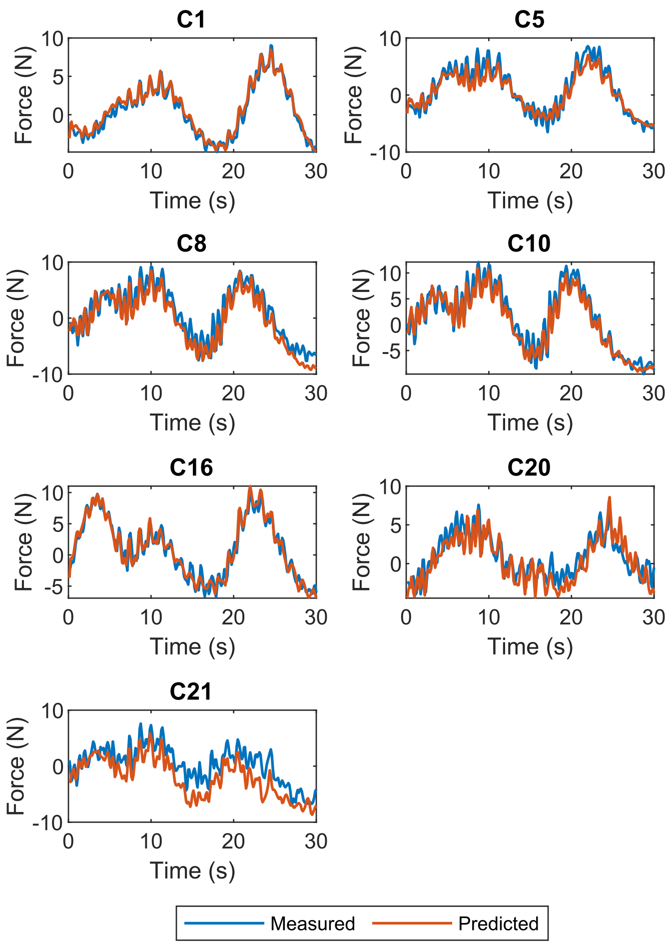

Fig. 9. Time series plot of predicted and measured force for test data when model input is 6-DOF motion in configuration 2.

Table 7
NRMSE Results for different input settings in FloWave. The generalized model is trained on all cases identified as “Train” and tested respectively on the cases identified as “Test”.

Case	Set	X only	XY	XYZ	6-DOF
F1	Train	0.9620	1.1428	0.9862	0.9346
F2	Test	0.3795	0.3857	0.3253	0.3314
F3	Train	0.3923	0.3847	0.3051	0.2911
F4	Train	0.4644	0.4744	0.4053	0.3862
F5	Train	0.5652	0.5219	0.4777	0.4655
F6	Train	0.5061	0.4867	0.4377	0.4221
F7	Test	0.4674	0.4534	0.4112	0.4011
F8	Train	0.5239	0.4946	0.4550	0.4465
F9	Test	0.7450	0.6843	0.6174	0.6070
F10	Train	0.9856	0.9125	0.9089	0.8800
Average		0.5991	0.5941	0.5330	**0.5165**

elevation, heave, pitch, surge, and bed force, for cases C3, C8, C10 and C11 in Fig. 11. It is clear that the surface elevations and M4 motions are practically identical demonstrating high repeatability of the conditions and associated hydrodynamic response of the M4 system. The bed force is substantially different due to the different mooring buoy configurations, with configuration 2 having larger low frequency forcing and substantially reduced forcing at the wave frequencies, owed to the reduced wave-induced forcing on the mooring buoy(s) themselves (Draycott et al., 2023). Hence, there is a different relationship between motion and force, a surrogate of a fault condition. It is worth noting that while spectral analysis can reveal differences in bed forces under various representative wave conditions, it is insufficient for condition

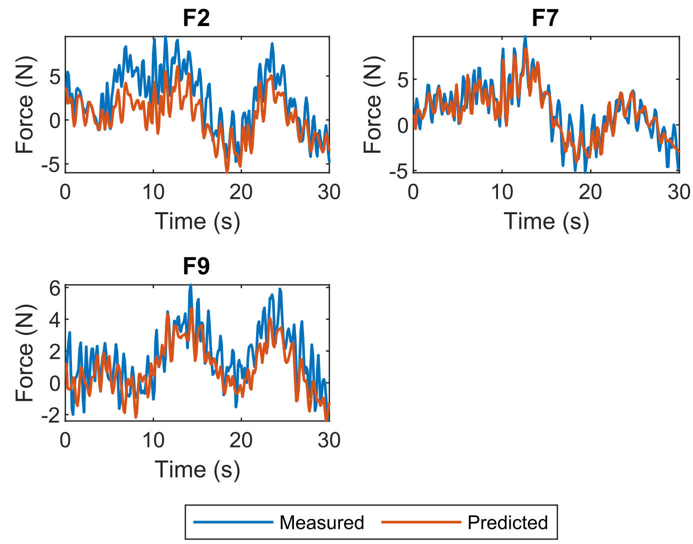

Fig. 10. Time series plot of predicted and measured force for test data when model input is 6-DOF motion in FloWave.

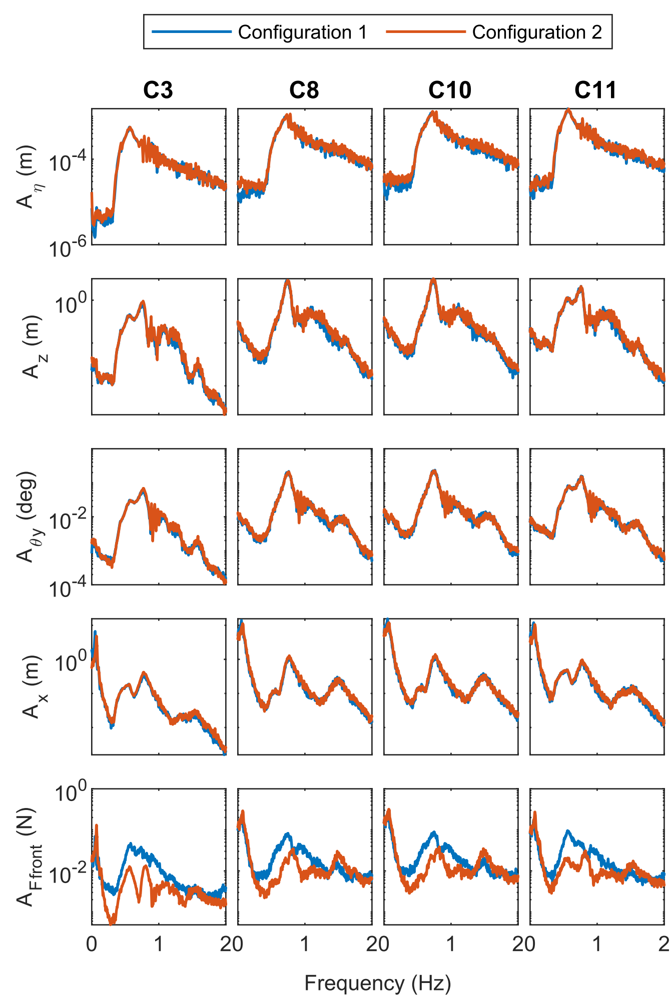

Fig. 11. FFTs of surface elevation (η), heave (z), pitch (θ_y), surge (x) and front bed force (F_{front}) for both Configuration 1 and Configuration 2. Shown for cases C3, C8, C10 and C11.

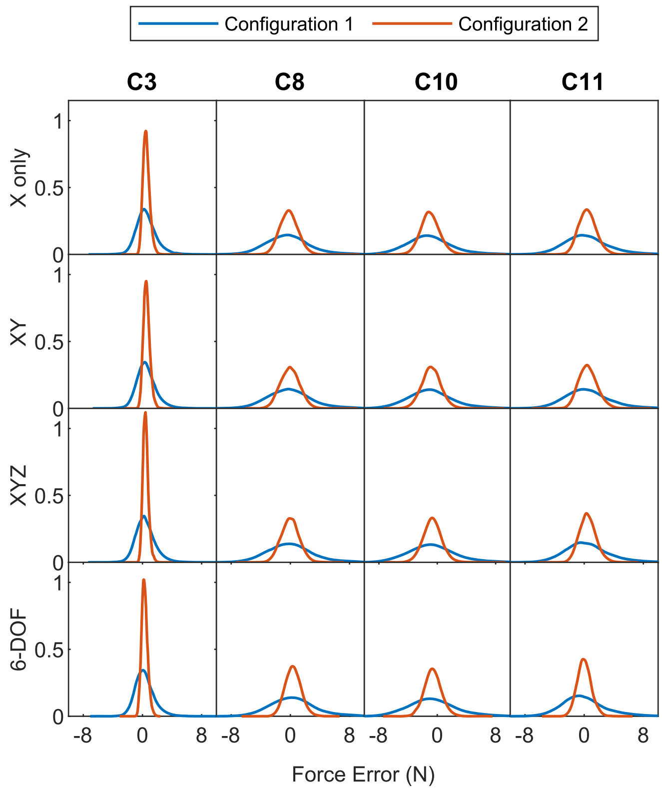

Fig. 12. Residual distributions for both Configurations 1 and Configurations 2. Shown for cases C3, C8, C10 and C11.

monitoring on its own. This limitation arises because spectral analysis requires comparisons under consistent wave conditions, which often vary in practice. To overcome this, the proposed method is designed to detect such differences under previously unseen wave conditions.

To assess the ability to identify these differences, the model is trained on twenty-two wave conditions from Configuration 2 and tested on sixteen wave conditions from Configuration 1, using data from the COAST laboratory. We take care to ensure that the modifications to float mean positions due to the change in mooring configuration are accounted for to enable consistency. Four models are developed using different input configurations: surge (X) motion only, planar (XY) motion, spatial (XYZ) motion, and 6-DOF motion. The performance evaluation involves analysing the residual distributions between measured and predicted forces for each input setting. Fig. 12 compare the residual distributions of the model predicted forces against the measured forces. Both configurations exhibit bell-shaped, approximately normal distributions; however, Configuration 1 displays flatter curves, whereas Configuration 2 yields narrower, more concentrated distributions across all sixteen cases. While these visual differences are apparent, a manual assessment remains impractical for rigorous analysis. For a quantitative comparison, NRMSE values are computed and presented in Table 8. The results, as expected, consistently show that Configuration 2 achieves lower NRMSE values than Configuration 1 across all wave conditions, as the generalized model was trained using Configuration 2 data and applied to Configuration 1 data. In all scenarios, the maximum NRMSE observed in the training dataset is lower than the minimum NRMSE in the test dataset. By applying NRMSE thresholds above 0.6 when the model input consists of surge (X) motion only or planar (XY) motion, and above 0.5 when the input includes spatial (XYZ) motion or full 6-DOF motion, the presence of a fault condition can be effectively defined. These results demonstrate that NRMSE thresholds can be used for condition monitoring applications as robust indicators that the dynamics of the system have changed. The experiments involve minor changes in the mooring system, and early-stage faults are successfully detected. However, in practical applications, the monitoring process is continuous and starts under healthy conditions, with the threshold set to a small value. If the detection results continuously exceed the threshold, a maintenance action is triggered. If the detection results only occasionally exceed the threshold, they are treated as false alarms, and the threshold can be further adjusted to reduce the false-alarm rate.

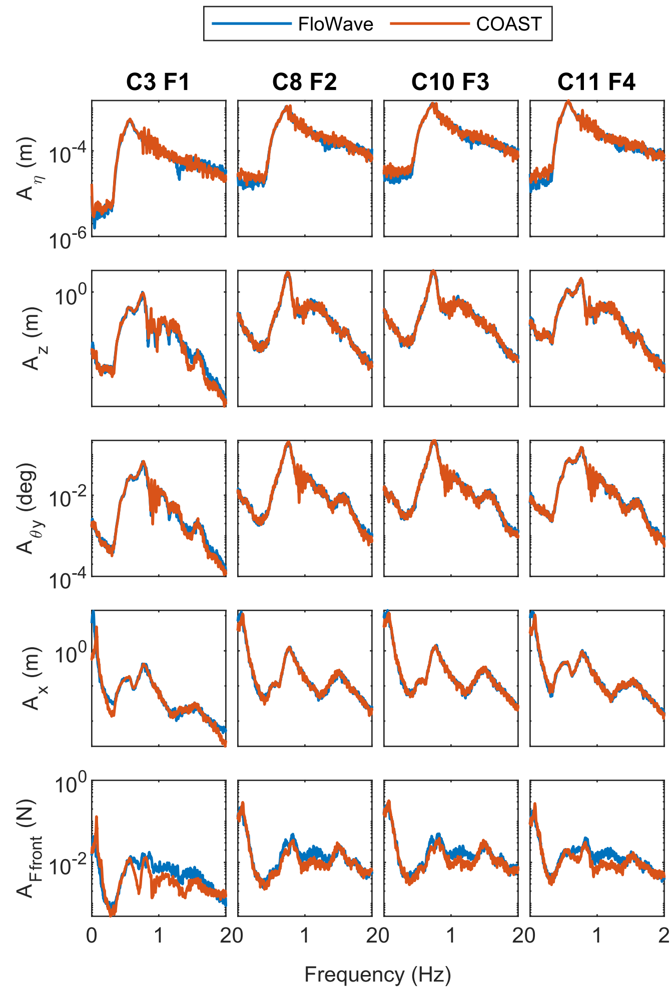

Fig. 13. FFTs of surface elevation (η), heave (z), pitch (θ_y), surge (x) and front bed force (F_{front}) for both FloWave and COAST. Shown for cases C3, C8, C10 and C11.

4.3.2. FloWave vs. COAST

The second experiment focuses on evaluating the nominally same configuration in different laboratory settings: FloWave and COAST. Although the mooring configuration was designed to be nominally the same, it is known that practically there will be several minor differences due to deviations in: wave generation, bed mounting positions, the elastic mooring lines used and line lengths, minor differences in buoyancy. To assess the physical differences we present FFTs of surface elevations, heave, pitch, surge and bed force, in Fig. 13. It is evident that there is excellent agreement in terms of the generated wave spectra along with very high similarity in terms of the heave and pitch of the M4 system. The M4 surge and associated bed force agree well over most of the spectrum, however, there are larger differences at low frequency, particularly the surge for case C3 (F1). There are also some smaller variations in the measured force around the wave frequencies, although much less than observed between configurations 1 and 2 (see Fig. 11). Overall, there are significant enough differences to treat this as

Table 8
NRMSE results for both Configurations 1 and Configurations 2.

Input	X only		XY		XYZ		6-DOF	
Case	Config 1 (Test)	Config 2 (Train)	Config 1 (Test)	Config 2 (Train)	Config 1 (Test)	Config 2 (Train)	Config 1 (Test)	Config 2 (Train)
C1	0.84	0.40	0.80	0.40	0.81	0.37	0.75	0.28
C2	0.95	0.45	0.91	0.43	0.92	0.38	0.89	0.33
C3	1.04	0.54 (max)	1.03	0.56 (max)	1.00	0.45 (max)	0.97	0.39
C4	0.66	0.33	0.66	0.33	0.66	0.31	0.65	0.25
C5	0.87	0.41	0.83	0.40	0.85	0.36	0.85	0.32
C6	0.98	0.42	0.94	0.44	0.93	0.38	0.93	0.38
C7	0.62 (min)	0.32	0.62 (min)	0.31	0.61 (min)	0.29	0.60	0.26
C8	0.67	0.26	0.67	0.27	0.69	0.26	0.69	0.24
C9	0.91	0.40	0.90	0.41	0.89	0.38	0.92	0.44 (max)
C10	0.64	0.29	0.63	0.28	0.64	0.26	0.65	0.23
C11	0.83	0.34	0.83	0.36	0.82	0.32	0.80	0.25
C12	0.64	0.34	0.63	0.32	0.63	0.30	0.60 (min)	0.22
C13	0.65	0.23	0.64	0.22	0.64	0.21	0.61	0.21
C14	0.71	0.32	0.72	0.34	0.71	0.31	0.63	0.21
C18	0.73	0.38	0.73	0.35	0.76	0.36	0.68	0.24
C20	0.78	0.39	0.77	0.37	0.80	0.36	0.79	0.30
Average	0.78	0.36	0.77	0.36	0.77	0.33	0.75	0.29

Table 9
NRMSE results for both FloWave and COAST.

Input	X only		XY		XYZ		6-DOF	
Case	FloWave (Test)	COAST (Train)	FloWave (Test)	COAST (Train)	FloWave (Test)	COAST (Train)	FloWave (Test)	COAST (Train)
C3 F1	1.08	0.54 (max)	1.03	0.56 (max)	1.01	0.45 (max)	1.07	0.39 (max)
C8 F2	0.53	0.26	0.53	0.27	0.51	0.26	0.51	0.24
C10 F3	0.50 (min)	0.29	0.48 (min)	0.28	0.46 (min)	0.26	0.45 (min)	0.23
C11 F4	0.68	0.34	0.67	0.36	0.65	0.32	0.62	0.25
Average	0.70	0.36	0.68	0.37	0.66	0.32	0.66	0.28

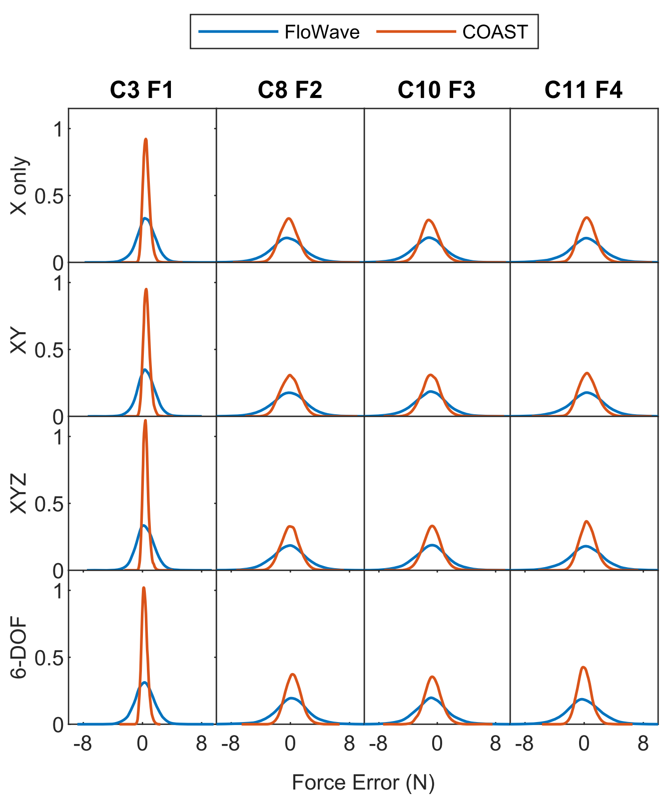

Fig. 14. Residual distributions for both FloWave and COAST.

another fault condition for testing the performance of the SI model for condition monitoring.

To assess the ability to identify these differences, the models are trained using data from the COAST laboratory and then applied to data collected from the FloWave laboratory. The four models used in this experiment are identical to those in the first experiment, with the same input settings. Fig. 14 compares the residual distributions between the model predicted forces and the measured forces. The data from the COAST laboratory exhibit narrower residual curves, while those from the FloWave laboratory show flatter distributions. The differences are generally small in most wave conditions, as both laboratories use the same physical configuration with minor differences. For a quantitative comparison, the NRMSE values are calculated and presented in Table 9. In all scenarios, the NRMSE values from the COAST laboratory are smaller than those from the FloWave laboratory. The maximum NRMSE in the training dataset and the minimum NRMSE in the test dataset are relatively close. The NRMSE ranges for the training and test datasets overlap when the input is limited to surge (X) motion only, but become increasingly separated as more input degrees of freedom are introduced. These results indicate that the proposed method remains effective for minor fault detection when the configuration has only minor differences.

5. Conclusion

In this paper, a cost-effective data-driven method is proposed for condition monitoring of mooring systems in a multi-float wave energy converter. First, several linear and nonlinear modelling methods are compared with Time Delay Neural Network (TDNN) models demonstrating the best performance. Subsequently, different training settings for the TDNN model are evaluated and performance sensitivity to the number of inputs is assessed where six-degree-of-freedom inputs are shown to be most effective. Generalized TDNN models are developed using data from both the COAST and FloWave facilities under various wave conditions and associated motion inputs, including challenging directionally spread and crossing wave conditions mimicking real ocean complexity. Finally, the TDNN models and residual-based analysis are used to distinguish between normal and altered conditions, using data under two surrogate fault scenarios: (i) two different mooring configurations in the same basin, and (ii) nominally the same mooring configuration in two basins. In the first scenario (two configurations in the Plymouth basin), the residual-based analysis successfully detects the small differences in mooring dynamics between the configurations and normalized root mean squared error thresholds can be effectively used to robustly identify the change in mooring dynamics. In the second scenario (FloWave versus COAST basins), the model detects the subtle differences arising from basin-specific hydrodynamic effects. In both scenarios, the ability to detect changes improves with increasing degrees-of-freedom included in the input, enabling earlier and more reliable fault identification. Since the identified models generalize across multiple wave conditions, the proposed method is able to detect such differences under unseen wave conditions. Overall, the method is shown as a highly promising approach for the condition monitoring of mooring systems for floating platforms, even for complex nonlinear systems in unseen and complex realistic sea states. In practice, such modelling may be used to assess changes in model structure during continuous monitoring; this will indicate deterioration or damage to a mooring for possible remedial action. Differentiating between mooring damage and effects of marine growth which will increase force is a further problem for future work.

Declaration of competing interest

The authors declare that they have no known competing financial interests or personal relationships that could have appeared to influence the work reported in this paper.

CRediT authorship contribution statement

Heng Yang: Writing - original draft; **Long Zhang:** Supervision; **Peter Stansby:** Writing - review & editing; **Samuel Draycott:** Writing - review & editing.

Acknowledgments

Funding from the EPSRC UK MoorWEC grant EP/V039946/1 is gratefully acknowledged. We would also like to thank the staff at the University of Plymouth COAST Laboratory, UK, and the staff at the FloWave Ocean Energy Research Racility, Edinburgh, UK, for their support.

References

Broomhead, D.S., Lowe, D., 1988. Multivariable functional interpolation and adaptive networks. Complex Syst. 2 (3), 321–355.
Burden, F., Winkler, D., 2009. Bayesian regularization of neural networks. In: Artificial Neural Networks: Methods and Applications. Humana Press, pp. 23–42.
Chung, M., Kim, S., Lee, K., Shin, D.H., 2020. Detection of damaged mooring line based on deep neural networks. Ocean Eng. 209, 107522.
Chung, W.C., Pestana, G.R., Kim, M., 2021. Structural health monitoring for TLP-FOWT (floating offshore wind turbine) tendon using sensors. Appl. Ocean Res. 113, 102740.
Coraddu, A., Oneto, L., Walker, J., Patryniak, K., Prothero, A., Collu, M., 2024. Floating offshore wind turbine mooring line sections health status nowcasting: from supervised shallow to weakly supervised deep learning. Mech. Syst. Signal Process. 216, 111446.
Draycott, S., Stansby, P., Gangqiang, L., 2023. Experimental measurements of two elastic taut-slack mooring configurations for the multi-float m4 WEC. Proceedings of the European Wave and Tidal Energy Conference 15.
Fathnejat, H., Nava, V., 2025. Data augmentation for damaged scenarios in floating offshore wind turbines: an approach based on diffusion architecture, hierarchical variational approximation and healthy data distribution. Eng. Comput. 41, 1979–1999.
Gnther, F., Fritsch, S., 2010. Neuralnet: training of neural networks. R J. 2.
Haider, R., Shi, W., Lin, Z., Xiao, Q., Zhang, W., Li, X., 2025. Dynamic response of floating offshore wind turbine to focused wave excitation. Phys. Fluids 37 (8), 082120.
Hashmani, M.A., Khatri, T.K., Koh, T.W., Rahim, L.A., Taib, H., Abdullah, N., 2024. A review of mooring monitoring methods for anomalies detection in thin mooring lines: challenges and future realms. In: 2024 International Conference on Electrical, Computer and Energy Technologies (ICECET, pp. 1–6.
Hochreiter, S., Schmidhuber, J., 1997. Long short-term memory. Neural Comput. 9 (8), 1735–1780.
Kvitrud, A., 2014. Lessons learned from norwegian mooring line failures 2010–2013. In: International Conference on Offshore Mechanics and Arctic Engineering. Volume 4A: Structures, Safety and Reliability. American Society of Mechanical Engineers, p. V04AT02A005.
Lee, K., Chung, M., Kim, S., Shin, D.H., 2021. Damage detection of catenary mooring line based on recurrent neural networks. Ocean Eng. 227, 108898.
Liu, W., Zhu, L., Feng, F., Zhang, W., Zhang, Q.-J., Lin, Q., Liu, G., 2020. A time delay neural network based technique for nonlinear microwave device modeling. Micromachines 11 (9), 831.
Ljung, L., 1999. System Identification: Theory for the User. Prentice Hall. 2nd edition.
Mao, Y., Duan, M., Men, H., Zheng, M., 2025. Local damage identification and nowcasting of mooring system using a noise-robust convmamba architecture. Mech. Syst. Signal Process. 224, 112092.
Müller, M.F., 1993. A scaled conjugate gradient algorithm for fast supervised learning. Neural Netw. 6 (4), 525–533.
Nayak, S., Choudhury, B.B., Lenka, S.K., 2016. Gradient descent with momentum based backpropagation neural network for selection of industrial robot. In: Proceedings of First International Conference on Information and Communication Technology for Intelligent Systems: Volume 1. Springer International Publishing, pp. 487–496.
Ren, Y., Shi, W., Venugopal, V., Zhang, L., Li, X., 2024. Experimental study of tendon failure analysis for a TLP floating offshore wind turbine. Appl. Energy 358, 122633.
Robitaille, B., Marcos, B., Veillette, M., Payre, G., 1996. Modified quasi-newton methods for training neural networks. Comput. Chem. Eng. 20 (9), 1133–1140.
Saad, A.M., Schopp, F., Barreira, R.A., Santos, I. H.F., Tannuri, E.A., Gomi, E.S., Costa, A. H.R., 2021. Using neural network approaches to detect mooring line failure. IEEE Access 9, 27678–27695.
Sapna, S., Tamilarasi, A., Kumar, M.P., 2008. Backpropagation learning algorithm based on levenberg-marquardt algorithm. Int. J. Comput. Sci. Netw. Secur. (IJCSNS) 8 (6), 243–247.
Specht, D.F., 1991. A general regression neural network. IEEE Trans. Neural Netw. 2 (6), 568–576.
Stansby, P., Draycott, S., 2024. M4 WEC Development and wave basin froude testing. Eur. J. Mech. B. Fluids 104, 182–193.
Sun, K., Xu, Z., Li, S., Jin, J., Wang, P., Yue, M., Li, C., 2023. Dynamic response analysis of floating wind turbine platform in local fatigue of mooring. Renew. Energy 204, 733–749.
Wang, T., Zhang, M., Ji, H., Liao, Q., 2020. Damage identification of mooring lines using RBF neural network. In: The Fourteenth ISOPE Pacific/Asia Offshore Mechanics Symposium, pp. ISOPE–P–20–159.
Zhang, L., Draycott, S., Stansby, P., 2024. System identification and generalisation of elastic mooring line forces on a multi-float wave energy converter platform in steep irregular waves. Mech. Syst. Signal Process 214, 111259.